Inhomogeneous Dielectric Induced Skew Modeling of Twinax Cables

Yuanzhuo Liu, *Student Member, IEEE*, Siqi Bai, *Member, IEEE*, Chaofeng Li, *Student Member, IEEE*, Vanine Sabino De Moura, *Student Member, IEEE*, Bichen Chen, *Member, IEEE*, Srinivas Venkataraman, Xu Wang, and DongHyun Kim, *Member, IEEE*

***Abstract*—To understand the skew in twinax cables of separately extrusion and co-extrusion design, the impact of inhomogeneous dielectric in copper twinax cables is analyzed, with an emphasis on signal integrity performance. The inhomogeneity is treated as a perturbation to the RLGC parameters, and analytical equations for the calculation of scattering parameters from RLGC parameters are derived to analyze the effects of this perturbation on signal integrity. The inhomogeneity leads to a modulation behavior in the scattering parameters, which decreases asymmetry-induced skew at high frequencies and eliminates the resonance of skew in the differential insertion loss. Mathematical analysis, physical explanation, and various design cases are presented for validation.**

***Index Terms*—Ethernet, inhomogeneous dielectric, PCI-express, RLGC parameters, SATA, scattering parameters, signal integrity, skew, twinax cable.**

I. Introduction

COPPER twinax cables are widely used for high-speed channels such as PCI-Express and Ethernet [1]. The time-domain intra-pair skew is often used as a specification to test the signal integrity performance of cables [2]. However, the skew may not correctly reflect the product's performance in real applications, because the skew is decreased at high frequencies [3].

Cables are extruded through two typical methods in industry: separately extrusion [4] and co-extrusion [5]. For separately extruded cables, two individually insulated conductors are wrapped together with shielding [6], as illustrated in Fig. 1(a). This type of cable is inhomogeneous because air pockets exist between the shielding and the dielectric insulator. The co-extruded cable shown in Fig. 1(b) has a single insulator extruded together with the two inner conductors. No air pockets exist in the co-extruded cable, and the dielectric is homogeneous.

Manuscript received 25 September 2022; revised 16 February 2023 and 10 May 2023; accepted 17 May 2023. Date of publication 22 May 2023; date of current version 6 June 2023. This work was supported by the National Science Foundation under Grant IIP-1440110 and Grant IIP-1916535 and in part by the Meta Platforms, California, USA. *(Corresponding author: Yuanzhuo Liu.)*

Yuanzhuo Liu, Siqi Bai, Chaofeng Li, Vanine Sabino De Moura, and DongHyun Kim are with the Electromagnetic Compatibility Laboratory, Missouri University of Science and Technology, Rolla, MO 65409 USA (e-mail: liuyuanz@mst.edu; sb2pc@mst.edu; clf83@mst.edu; vsdhb@mst.edu; dkim@mst.edu).

Bichen Chen, Srinivas Venkataraman, and Xu Wang are with the Facebook, Inc., Menlo Park, CA 94025 USA (e-mail: bcchen@fb.com; srinivasv@fb.com; xuwang@fb.com).

Digital Object Identifier 10.1109/TSIPI.2023.3278613

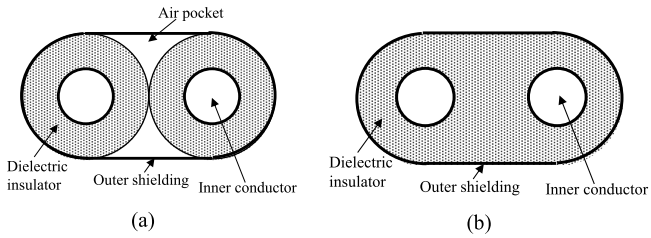

Fig. 1. Cross-section of copper twinax cables. (a) Separately extruded cable. (b) Co-extruded cable.

Separately extruded cables were often misconceived to have greater skew-induced differential insertion loss resonance due to minor asymmetries in the diameters of the coextruded conductors and the differences in permittivity of the insulators [7]. In addition, the lower manufacturing cost of the separately extruded cables compared to coextruded cables was another factor to be misconceived to have higher skew-induced resonance in differential loss. Skew leads to a resonance in the differential insertion loss at a frequency equal to 1/(2 skew) [8], and therefore lower skew is desired to minimize unwanted resonances in differential insertion loss at operating frequency. Contrary to the misconception, in separately extruded cables, the inhomogeneity can help decrease asymmetry-induced skew at high frequencies and eliminates the resonance due to skew in the differential insertion loss.

The inhomogeneity in a dielectric material can lead to modulation behavior in the scattering parameters (*S*-parameters) [9]. Similar to the case of a microstrip [10], the phase velocities of odd and even modes differ due to the dielectric inhomogeneity [11]. Inhomogeneity introduces a relatively small change in the capacitance matrix [12], which leads to modulation between propagation constants and significantly changes the behavior of *S*-parameters [13]. Because the magnitude of the change in the capacitance matrix is relatively small, this change is referred to as perturbation in capacitance.

To analyze the effect of inhomogeneity of the dielectric on the signal integrity performance of a cable, an analytical equation to calculate *S*-parameters from RLGC parameters is derived. Calculation of *S*-parameters from RLGC parameters for multiconductor transmission lines commonly requires the calculation of the hyperbolic function of the matrix [14]. The matrix hyperbolic function is calculated by the summation of an infinite series, thus increasing the complexity of perturbation analysis

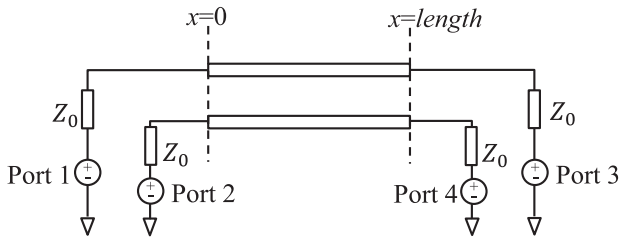

Fig. 2. Coupled two-dimensional transmission line.

[15]. Therefore, the perturbation analysis is proposed based on solving eigenvalues and eigenvectors [16]. *S*-parameters can be calculated from elements of the RLGC parameters without a need for calculating matrix hyperbolic functions or any other infinite series. This work assumes that the cable is an ideal transmission line, which is invariant along the transmission direction.

In this study, we propose the physical explanation for reduced high-frequency skew in an inhomogeneous dielectric material, and root cause for better performance in differential insertion loss of separately extruded cables when compared to co-extruded cables, despite the higher skew in separately extruded twinax cables. Mathematical analysis, a physical explanation, and various design cases are presented for explanation. For illustration purposes, symmetric cables with and without inhomogeneity are compared. Then asymmetric cables with and without inhomogeneity are compared.

The method for calculating *S*-parameters from RLGC parameters is introduced in Section II. Analysis of the inhomogeneous dielectric-induced modulation is shown in Section III, with numerical examples in Section IV. Analysis of asymmetry-induced skew is discussed in Section V and is followed by the conclusion section.

II. Calculating the *S*-Parameter From RLGC Matrix

The governing partial differential equation (PDE) of a two-dimensional coupled transmission line, as shown in Fig. 2, can be written as

$$\begin{bmatrix} \frac{d^2V_1}{dx^2} \\ \frac{d^2V_2}{dx^2} \end{bmatrix} = \left(\begin{bmatrix} R_{11} & R_{12} \\ R_{21} & R_{22} \end{bmatrix} + \begin{bmatrix} sL_{11} & sL_{12} \\ sL_{21} & sL_{22} \end{bmatrix} \right) \times \left(\begin{bmatrix} G_{11} & G_{12} \\ G_{21} & G_{22} \end{bmatrix} + \begin{bmatrix} sC_{11} & sC_{12} \\ sC_{21} & sC_{22} \end{bmatrix} \right) \begin{bmatrix} V_1 \\ V_2 \end{bmatrix} \quad (1)$$

$$\begin{bmatrix} \frac{dV_1}{dx} \\ \frac{dV_2}{dx} \end{bmatrix} + \left(\begin{bmatrix} R_{11} & R_{12} \\ R_{21} & R_{22} \end{bmatrix} + \begin{bmatrix} sL_{11} & sL_{12} \\ sL_{21} & sL_{22} \end{bmatrix} \right) \begin{bmatrix} I_1 \\ I_2 \end{bmatrix} = 0 \quad (2)$$

where the voltages V_1 and V_2, and the currents I_1 and I_2 are in the frequency domain; s is the Laplace operator; and the $\boldsymbol{R}$, $\boldsymbol{L}$, $\boldsymbol{G}$, and $\boldsymbol{C}$ matrix are frequency dependent. Full definitions of $\boldsymbol{P} = (\boldsymbol{R} + s\boldsymbol{L})(\boldsymbol{G} + s\boldsymbol{C})$, (1) is as follows:

$$\begin{aligned} \frac{d^2V_1}{dx^2} &= P_{11}V_1 + P_{12}V_2 \\ \frac{d^2V_2}{dx^2} &= P_{21}V_1 + P_{22}V_2. \end{aligned} \quad (3)$$

The following set of equations is assessed for the solution:

$$\begin{aligned} V_1(x) &= m_1 \sin h(\gamma x) \\ V_2(x) &= m_2 \sin h(\gamma x) \end{aligned} \quad (4)$$

where m_1, m_2, and γ are constants to be determined later.

By substituting (4) into (3), and a set of linear equations for unknowns m_1 and m_2, the following are obtained:

$$\begin{aligned} \left(P_{11} - \gamma^2\right) m_1 + P_{12} m_2 &= 0 \\ P_{21} m_1 + \left(P_{22} - \gamma^2\right) m_2 &= 0. \end{aligned} \quad (5)$$

For (5) to have a nontrivial solution, the determinant of the coefficient matrix must be 0, thus leading to the following:

$$\begin{aligned} &\det \begin{vmatrix} P_{11} - \gamma^2 & P_{12} \\ P_{21} & P_{22} - \gamma^2 \end{vmatrix} \\ &= \left(P_{11} - \gamma^2\right)\left(P_{22} - \gamma^2\right) - P_{12}P_{21} = 0. \end{aligned} \quad (6)$$

The two roots γ_1^2 and γ_2^2 of (6) are the eigenvalues of $\boldsymbol{P}$, and the expressions for γ_1^2 and γ_2^2 are:

$$\begin{aligned} \gamma_1^2 &= \frac{P_{11} + P_{22} - \sqrt{(P_{11} + P_{22})^2 - 4(P_{11}P_{22} - P_{12}P_{21})}}{2} \\ \gamma_2^2 &= \frac{P_{11} + P_{22} + \sqrt{(P_{11} + P_{22})^2 - 4(P_{11}P_{22} - P_{12}P_{21})}}{2}. \end{aligned} \quad (7)$$

The corresponding eigenvectors are:

$$\begin{bmatrix} 1 \\ m_{21} \end{bmatrix} \begin{bmatrix} m_{12} \\ 1 \end{bmatrix} \quad (8)$$

where the expressions for m_{12} and m_{21} are as follows:

$$\begin{aligned} m_{21} &= \begin{cases} \frac{\gamma_1^2 - P_{11}}{P_{12}}, & \text{if } P_{12} \neq 0 \\ 0, & \text{if} P_{12} = 0 \end{cases} \\ m_{12} &= \begin{cases} \frac{\gamma_2^2 - P_{22}}{P_{21}}, & \text{if } P_{21} \neq 0 \\ 0, & \text{if } P_{21} = 0 \end{cases}. \end{aligned} \quad (9)$$

Because the PDE (1) is second order, two sets of solutions exist. The solution set (10) is chosen as the second trial solution, and the resulting eigenvalues and eigenvectors are the same as in (7)–(9).

$$\begin{aligned} V_1(x) &= m_1 \cos h(\gamma x) \\ V_2(x) &= m_2 \cos h(\gamma x). \end{aligned} \quad (10)$$

The solution of the PDE (1) is a combination of the two sets of trial solutions and can be written as (11), where k_1, k_2, and n_1 are constants to be determined by the boundary conditions

$$\begin{bmatrix} V_1 \\ V_2 \end{bmatrix} = \begin{bmatrix} 1 & m_{12} \\ m_{21} & 1 \end{bmatrix} \begin{bmatrix} \sin h(\gamma_1 x) & 0 \\ 0 & \sin h(\gamma_2 x) \end{bmatrix} \begin{bmatrix} k_1 \\ k_2 \end{bmatrix} + \begin{bmatrix} 1 & m_{12} \\ m_{21} & 1 \end{bmatrix} \begin{bmatrix} \cos h(\gamma_1 x) & 0 \\ 0 & \cos h(\gamma_2 x) \end{bmatrix} \begin{bmatrix} n_1 \\ n_2 \end{bmatrix}. \quad (11)$$

By substituting (11) into (2), the solutions for the current can be obtained:

$$\begin{aligned}\begin{bmatrix} I_1 \\ I_2 \end{bmatrix} &= -\begin{bmatrix} R_{11}+sL_{11} & R_{12}+sL_{12} \\ R_{21}+sL_{21} & R_{22}+sL_{22} \end{bmatrix}^{-1} \begin{bmatrix} 1 & m_{12} \\ m_{21} & 1 \end{bmatrix} \\ &\times \begin{bmatrix} \gamma_1 \cos h(\gamma_1 x) & 0 \\ 0 & \gamma_2 \cos h(\gamma_2 x) \end{bmatrix} \begin{bmatrix} k_1 \\ k_2 \end{bmatrix} \\ &- \begin{bmatrix} R_{11}+sL_{11} & R_{12}+sL_{12} \\ R_{21}+sL_{21} & R_{22}+sL_{22} \end{bmatrix}^{-1} \begin{bmatrix} 1 & m_{12} \\ m_{21} & 1 \end{bmatrix} \\ &\times \begin{bmatrix} \gamma_1 \sin h(\gamma_1 x) & 0 \\ 0 & \gamma_2 \sin h(\gamma_2 x) \end{bmatrix} \begin{bmatrix} n_1 \\ n_2 \end{bmatrix}. \end{aligned} \tag{12}$$

Next, after application of the boundary conditions at $x = 0$, (13) can be obtained

$$\begin{aligned}\begin{bmatrix} V_1(0) \\ V_2(0) \end{bmatrix} &= \begin{bmatrix} 1 & m_{12} \\ m_{21} & 1 \end{bmatrix} \begin{bmatrix} n_1 \\ n_2 \end{bmatrix} \\ \begin{bmatrix} I_1(0) \\ I_2(0) \end{bmatrix} &= -\begin{bmatrix} R_{11}+sL_{11} & R_{12}+sL_{12} \\ R_{21}+sL_{21} & R_{22}+sL_{22} \end{bmatrix}^{-1} \begin{bmatrix} 1 & m_{12} \\ m_{21} & 1 \end{bmatrix} \\ &\times \begin{bmatrix} \gamma_1 & 0 \\ 0 & \gamma_2 \end{bmatrix} \begin{bmatrix} k_1 \\ k_2 \end{bmatrix}. \end{aligned} \tag{13}$$

From (13), the unknown constants k_1, k_2, n_1, and n_2 can be determined. Thus, the solutions can be written as

$$\begin{aligned}\begin{bmatrix} V_1(x) \\ V_2(x) \end{bmatrix} &= -\begin{bmatrix} 1 & m_{12} \\ m_{21} & 1 \end{bmatrix} \begin{bmatrix} \frac{\sin h(\gamma_1 x)}{\gamma_1} & 0 \\ 0 & \frac{\sin h(\gamma_2 x)}{\gamma_2} \end{bmatrix} \\ &\times \begin{bmatrix} 1 & m_{12} \\ m_{21} & 1 \end{bmatrix}^{-1} \begin{bmatrix} R_{11}+sL_{11} & R_{12}+sL_{12} \\ R_{21}+sL_{21} & R_{22}+sL_{22} \end{bmatrix} \\ &\begin{bmatrix} I_1(0) \\ I_2(0) \end{bmatrix} \begin{bmatrix} 1 & m_{12} \\ m_{21} & 1 \end{bmatrix} \begin{bmatrix} \cos h(\gamma_1 x) & 0 \\ 0 & \cos h(\gamma_2 x) \end{bmatrix} \\ &\begin{bmatrix} 1 & m_{12} \\ m_{21} & 1 \end{bmatrix}^{-1} \begin{bmatrix} V_1(0) \\ V_2(0) \end{bmatrix} \end{aligned} \tag{14}$$

$$\begin{aligned}\begin{bmatrix} I_1(x) \\ I_2(x) \end{bmatrix} &= \begin{bmatrix} R_{11}+sL_{11} & R_{12}+sL_{12} \\ R_{21}+sL_{21} & R_{22}+sL_{22} \end{bmatrix}^{-1} \\ &\begin{bmatrix} 1 & m_{12} \\ m_{21} & 1 \end{bmatrix} \times \begin{bmatrix} \cos h(\gamma_1 x) & 0 \\ 0 & \cos h(\gamma_2 x) \end{bmatrix} \\ &\begin{bmatrix} 1 & m_{12} \\ m_{21} & 1 \end{bmatrix}^{-1} \times \begin{bmatrix} R_{11}+sL_{11} & R_{12}+sL_{12} \\ R_{21}+sL_{21} & R_{22}+sL_{22} \end{bmatrix} \\ &\begin{bmatrix} I_1(0) \\ I_2(0) \end{bmatrix} - \begin{bmatrix} R_{11}+sL_{11} & R_{12}+sL_{12} \\ R_{21}+sL_{21} & R_{22}+sL_{22} \end{bmatrix}^{-1} \\ &\times \begin{bmatrix} 1 & m_{12} \\ m_{21} & 1 \end{bmatrix} \begin{bmatrix} \gamma_1 \sin h(\gamma_1 x) & 0 \\ 0 & \gamma_2 \sin h(\gamma_2 x) \end{bmatrix} \\ &\times \begin{bmatrix} 1 & m_{12} \\ m_{21} & 1 \end{bmatrix}^{-1} \begin{bmatrix} V_1(0) \\ V_2(0) \end{bmatrix}. \end{aligned} \tag{15}$$

Finally, from (14) and (15), the ***ABCD*** matrix can be derived:

$$\begin{aligned}\boldsymbol{A} &= \begin{bmatrix} 1 & m_{12} \\ m_{21} & 1 \end{bmatrix} \begin{bmatrix} \cos h(\gamma_1 x) & 0 \\ 0 & \cos h(\gamma_2 x) \end{bmatrix} \\ &\begin{bmatrix} 1 & m_{12} \\ m_{21} & 1 \end{bmatrix}^{-1} \end{aligned} \tag{16}$$

$$\begin{aligned}\boldsymbol{B} &= \begin{bmatrix} 1 & m_{12} \\ m_{21} & 1 \end{bmatrix} \begin{bmatrix} \frac{\sin h(\gamma_1 x)}{\gamma_1} & 0 \\ 0 & \frac{\sin h(\gamma_2 x)}{\gamma_2} \end{bmatrix} \\ &\times \begin{bmatrix} 1 & m_{12} \\ m_{21} & 1 \end{bmatrix}^{-1} \begin{bmatrix} R_{11}+sL_{11} & R_{12}+sL_{12} \\ R_{21}+sL_{21} & R_{22}+sL_{22} \end{bmatrix} \end{aligned} \tag{17}$$

$$\begin{aligned}\boldsymbol{C} &= \begin{bmatrix} R_{11}+sL_{11} & R_{12}+sL_{12} \\ R_{21}+sL_{21} & R_{22}+sL_{22} \end{bmatrix}^{-1} \begin{bmatrix} 1 & m_{12} \\ m_{21} & 1 \end{bmatrix} \\ &\times \begin{bmatrix} \gamma_1 \sin h(\gamma_1 x) & 0 \\ 0 & \gamma_2 \sin h(\gamma_2 x) \end{bmatrix} \begin{bmatrix} 1 & m_{12} \\ m_{21} & 1 \end{bmatrix}^{-1} \end{aligned} \tag{18}$$

$$\begin{aligned}\boldsymbol{D} &= \begin{bmatrix} R_{11}+sL_{11} & R_{12}+sL_{12} \\ R_{21}+sL_{21} & R_{22}+sL_{22} \end{bmatrix}^{-1} \begin{bmatrix} 1 & m_{12} \\ m_{21} & 1 \end{bmatrix} \\ &\times \begin{bmatrix} \cos h(\gamma_1 x) & 0 \\ 0 & \cos h(\gamma_2 x) \end{bmatrix} \begin{bmatrix} 1 & m_{12} \\ m_{21} & 1 \end{bmatrix}^{-1} \\ &\begin{bmatrix} R_{11}+sL_{11} & R_{12}+sL_{12} \\ R_{21}+sL_{21} & R_{22}+sL_{22} \end{bmatrix}. \end{aligned} \tag{19}$$

The scattering parameters can be obtained from the ***ABCD*** matrix [18]

$$\begin{aligned}\begin{bmatrix} S_{13} & S_{14} \\ S_{23} & S_{24} \end{bmatrix} &= 2\left(A + \frac{B}{Z_0} + Z_0 C + D\right)^{-1} \\ \begin{bmatrix} S_{11} & S_{12} \\ S_{21} & S_{22} \end{bmatrix} &= \left(A + \frac{B}{Z_0} + Z_0 C + D\right)^{-1} \\ &\times \left(A + \frac{B}{Z_0} - Z_0 C - D\right). \end{aligned} \tag{20}$$

Equation (20) is a rigorous analytical expression for calculating the S-parameter from RLGC parameters of a two-dimensional coupled transmission line. Then the *S*-parameters can be calculated without solving the hyperbolic function of a matrix or other infinite series. Each element in (16)–(19) can be calculated from the RLGC matrix explicitly, thus allowing us to investigate how a perturbation in the ***C*** matrix affects the *S*-parameters, as shown in the following section.

III. Perturbation Analysis of Inhomogeneity

The co-extruded cable with a homogeneous and symmetric dielectric is discussed first. For the separately extruded cable with air pockets, the inhomogeneity is treated as a perturbation to the ***C*** matrix and then illustrates how a relatively small inhomogeneity can significantly change the S-parameter. For simplicity, all cases discussed here are lossless. For lossless transmission lines, ***R*** and ***G*** are zero, and ***L*** and ***C*** are constant over the frequency.

A. Special Case: Homogeneous and Symmetric

For homogeneous, lossless, and symmetric co-extruded cables, $L_{11}C_{12} + L_{12}\ C_{22} = 0$, and the ***P*** matrix becomes a diagonal matrix with two equal diagonal elements. The two propagation constants are equal

$$\gamma_1 = \gamma_2 = \gamma = s\sqrt{L_{11}C_{11} + L_{12}C_{21}}. \tag{21}$$

For simplicity, identity matrix $\boldsymbol{I}$ is chosen as the eigenmatrix of the diagonal matrix $\boldsymbol{P}$. Therefore, the ***ABCD*** matrix can be written as

$$\boldsymbol{A} = \begin{bmatrix} \cos h(\gamma x) & 0 \\ 0 & \cos h(\gamma x) \end{bmatrix} \tag{22}$$

$$\boldsymbol{B} = \frac{\sin h(\gamma x)}{\gamma} \begin{bmatrix} sL_{11} & sL_{12} \\ sL_{21} & sL_{22} \end{bmatrix} \tag{23}$$

$$\boldsymbol{C} = -\gamma_1 \sin h(\gamma x) \begin{bmatrix} sL_{11} & sL_{12} \\ sL_{21} & sL_{22} \end{bmatrix}^{-1} \tag{24}$$

$$\boldsymbol{D} = \begin{bmatrix} \cos h(\gamma x) & 0 \\ 0 & \cos h(\gamma x) \end{bmatrix}. \tag{25}$$

Of note, γ is an imaginary number. Thus, $\cosh(\gamma x) = \cos(|\gamma x|)$, and $\sinh(\gamma x) = i\sin(|\gamma x|)$. Consequently, each element of the ***ABCD*** matrix is periodic, and the period frequency is as follows:

$$f_{\text{period}} = \frac{1}{\text{Length}\sqrt{L_{11}C_{11} + L_{12}C_{21}}} \tag{26}$$

where Length is the total length of the transmission line. Each element of the ***ABCD*** parameters has the same period and thus the same for the *S*-parameters.

B. Perturbation of Air Pockets

We now consider a lossless two-dimensional symmetric separately extruded cable with air pockets. Because of the inhomogeneity, matrix $\boldsymbol{P}$ is not a diagonal matrix and can be written as

$$\begin{aligned} \boldsymbol{P} &= s^2 \begin{bmatrix} L_{11}C_{11} + L_{12}C_{21} & L_{11}C_{12} + L_{12}C_{22} \\ L_{21}C_{11} + L_{22}C_{21} & L_{21}C_{12} + L_{22}C_{22} \end{bmatrix} \\ &= \begin{bmatrix} p & e \\ e & \end{bmatrix} \end{aligned} \tag{27}$$

where $p = L_{11}\ C_{11} + L_{12}\ C_{21} = L_{21}\ C_{12} + L_{22}C_{22}$, $e = L_{11}\ C_{12} + L_{12}\ C_{22} = L_{21}\ C_{11} + L_{22}C_{21}$, and $|p| \gg |e|$. The two eigenvalues are

$$\begin{aligned} \gamma_1'^2 &= p - e \\ \gamma_2'^2 &= p + e. \end{aligned} \tag{28}$$

The two corresponding eigenvectors are:

$$\begin{bmatrix} 1 & \\ m_{21} & \end{bmatrix} \begin{bmatrix} m_{12} \\ 1 \end{bmatrix} = \begin{bmatrix} 1 & \\ -1 & \end{bmatrix} \begin{bmatrix} 1 \\ 1 \end{bmatrix}. \tag{29}$$

The $\boldsymbol{A}$ matrix is: (30) shown at the bottom of this page.

Each element of the $\boldsymbol{A}$ matrix has a fast-switching component $(\gamma'_1 + \gamma'_2)/2$ and a slow modulation component$(-\gamma'_1 + \gamma'_2)/2$. With Taylor's expansion, the two propagation constants can be written as

$$\begin{aligned} \gamma'_1 &= \sqrt{p - e} \approx \sqrt{p}\left(1 - \frac{1}{2}\frac{e}{p}\right) \\ \gamma'_2 &= \sqrt{p + e} \approx \sqrt{p}\left(1 + \frac{1}{2}\frac{e}{p}\right) \end{aligned} \tag{31}$$

$$f_{\text{modulation}} = \frac{\sqrt{L_{11}C_{11} + L_{12}C_{21}}}{\text{Length}\,(L_{11}C_{12} + L_{12}C_{22})}. \tag{32}$$

The period of the modulation can be obtained with (32). The *S*-parameters are also periodic and modulated. At one-quarter of the modulation frequency, $\boldsymbol{A}$ and $\boldsymbol{D}$ become

$$\boldsymbol{A} = \boldsymbol{D} = \begin{bmatrix} 0 & i\sin h(\frac{\gamma'_1+\gamma'_2}{2}x) \\ i\sin h(\frac{\gamma'_1+\gamma'_2}{2}x) & 0 \end{bmatrix} \tag{33}$$

and the diagonal elements are 0. Meanwhile, $\boldsymbol{B}$ and $\boldsymbol{C}_{ABCD}$ become:

$$\begin{aligned} \boldsymbol{B} &\approx \frac{\sin h(\gamma'_1 x)}{2\gamma'_1} \begin{bmatrix} \frac{\gamma'_2-\gamma'_1}{\gamma'_2} & \frac{-\gamma'_1-\gamma'_2}{\gamma'_2} \\ \frac{-\gamma'_1-\gamma'_2}{\gamma'_2} & \frac{\gamma'_2-\gamma'_1}{\gamma'_2} \end{bmatrix} \begin{bmatrix} sL_{11} & sL_{12} \\ sL_{21} & sL_{22} \end{bmatrix} \\ &\approx -\frac{\sin h(\gamma'_1 x)}{\gamma'_1} \begin{bmatrix} 0 & 1 \\ 1 & 0 \end{bmatrix} \begin{bmatrix} sL_{11} & sL_{12} \\ sL_{21} & sL_{22} \end{bmatrix} \\ &= -\frac{\sin h(\gamma'_1 x)}{\gamma'_1} \begin{bmatrix} sL_{21} & sL_{22} \\ sL_{11} & sL_{12} \end{bmatrix} \end{aligned} \tag{34}$$

$$\begin{aligned} \boldsymbol{C} &\approx \sin h(\gamma'_1 x) \begin{bmatrix} sL_{11} & sL_{12} \\ sL_{21} & sL_{22} \end{bmatrix}^{-1} \begin{bmatrix} \frac{\gamma'_1-\gamma'_2}{2} & \frac{-\gamma'_1-\gamma'_2}{2} \\ \frac{-\gamma'_1-\gamma'_2}{2} & \frac{\gamma'_1-\gamma'_2}{2} \end{bmatrix} \\ &\approx -\gamma'_1 \sin h(\gamma'_1 x) \begin{bmatrix} sL_{11} & sL_{12} \\ sL_{21} & sL_{22} \end{bmatrix}^{-1} \begin{bmatrix} 0 & 1 \\ 1 & 0 \end{bmatrix} \\ &= \frac{s\gamma'_1 \sin h(\gamma'_1 x)}{L_{11}^2 - L_{12}^2} \begin{bmatrix} L_{12} & -L_{22} \\ -L_{11} & L_{21} \end{bmatrix} \end{aligned} \tag{35}$$

$$\begin{aligned} \boldsymbol{A} &= \begin{bmatrix} 1 & m_{12} \\ m_{21} & 1 \end{bmatrix} \begin{bmatrix} \cos h(\gamma'_1 x) & 0 \\ 0 & \cos h(\gamma'_2 x) \end{bmatrix} \begin{bmatrix} 1 & m_{12} \\ m_{21} & 1 \end{bmatrix}^{-1} \\ &= \begin{bmatrix} 1 & 1 \\ -1 & 1 \end{bmatrix} \begin{bmatrix} \cos h(\gamma'_1 x) & 0 \\ 0 & \cos h(\gamma'_2 x) \end{bmatrix} \begin{bmatrix} 1 & 1 \\ -1 & 1 \end{bmatrix}^{-1} \\ &= \begin{bmatrix} \frac{\cos h(\gamma'_1 x) + \cos h(\gamma'_2 x)}{2} & \frac{-\cosh(\gamma'_1 x) + \cos h(\gamma'_2 x)}{2} \\ \frac{-\cos h(\gamma'_1 x) + \cos h(\gamma'_2 x)}{2} & \frac{\cos h(\gamma'_1 x) + \cos h(\gamma'_2 x)}{2} \end{bmatrix} \\ &= \begin{bmatrix} \cos h(\frac{\gamma'_1+\gamma'_2}{2}x)\cos h(\frac{\gamma'_1-\gamma'_2}{2}x) & \sin h(\frac{\gamma'_1+\gamma'_2}{2}x)\sin h(\frac{-\gamma'_1+\gamma'_2}{2}x) \\ \sin h(\frac{\gamma'_1+\gamma'_2}{2}x)\sin h(\frac{-\gamma'_1+\gamma'_2}{2}x) & \cos h(\frac{\gamma'_1+\gamma'_2}{2}x)\cos h(\frac{\gamma'_1-\gamma'_2}{2}x) \end{bmatrix}. \end{aligned} \tag{30}$$

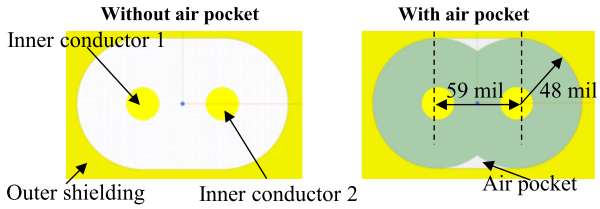

Fig. 3. Test geometries for a twin-axial cable with and without air pockets.

with the off-diagonal elements much greater than the diagonal elements. We now substitute (33)–(35) into (20), and obtain the insertion loss and far-end crosstalk

$$\begin{bmatrix} S_{13} & S_{14} \\ S_{23} & S_{24} \end{bmatrix} = 2\left(A + \frac{B}{Z_0} + Z_0 C_{ABCD} + D\right)^{-1}$$
$$= 2\begin{bmatrix} u & v \\ v & u \end{bmatrix}^{-1}$$
$$= \frac{2}{v^2 - u^2}\begin{bmatrix} -u & v \\ v & -u \end{bmatrix} \tag{36}$$

where u and v are

$$u = -\frac{\sin h(\gamma'_1 x)}{Z_0 \gamma'_1} sL_{21} + \frac{s\gamma'_1 \sin h(\gamma'_1 x) Z_0}{L_{11}^2 - L_{12}^2} sL_{21} \tag{37}$$

$$v = 2i \sin h\left(\frac{\gamma'_1 + \gamma'_2}{2} x\right) - \frac{\sin h(\gamma'_1 x)}{Z_0 \gamma'_1} sL_{22}$$
$$- \frac{s\gamma'_1 \sin h(\gamma'_1 x) Z_0}{L_{11}^2 - L_{12}^2} sL_{22} \tag{38}$$

and $|u| \ll |v|$. Therefore, at one-quarter of the modulation frequency, the insertion loss terms S_{13} and S_{24} are close to 0, and the far-end crosstalk terms S_{14} and S_{23} are close to 1.

IV. Numerical Examples

The single-ended *S*-parameters of these two cable types significantly differ because of the inhomogeneity in the dielectric introduced by the air pockets. To illustrate this phenomenon, we use two simulation model geometries (see Fig. 3) as examples. The two simulation models are identical except for the presence or absence of air pockets. The example twin-axial cables have two inner conductors inside an outer shielding. The radius of the inner conductor is 12 mil, and all other dimensions are indicated in the figure. The permittivity of the dielectric is 2.1, and the permeability is 1. All conductors and dielectrics are assumed to be lossless for simplicity. The cross-section is simulated in ANSYS 2D Extractor [19] for the RLGC parameters. The ***R*** and ***G*** matrices are 0, because the examples are lossless. The simulated ***L*** and ***C*** matrices for the two cases are listed in Table I. The ***L*** matrix for the two cases is identical because the air pocket has the same permeability as the dielectric. The air pocket changes the ***C*** matrix slightly. As described, the air pocket is a perturbation to the ***C*** matrix.

The simulated RLGC parameters are substituted into (20) to calculate the *S*-parameters for a 1-meter cable with 50 Ω port impedance. The results are compared with ANSYS exported *S*-parameters in Fig. 4. The *S*-parameters calculated by (20) are identical to the results simulated by ANSYS, thus validating the proposed method for calculating *S*-parameters.

TABLE I
Simulated **L** and **C** Matrix Without and With Pocktets

	L matrix (nH/m)	***C*** matrix (pF/m)
Without air pockets	$\begin{bmatrix} 296.0 & 50.1 \\ 50.1 & 296.0 \end{bmatrix}$	$\begin{bmatrix} 81.26 & -13.76 \\ -13.76 & 81.26 \end{bmatrix}$
With air pockets	$\begin{bmatrix} 296.0 & 50.1 \\ 50.1 & 296.0 \end{bmatrix}$	$\begin{bmatrix} 80.46 & -14.38 \\ -14.38 & 80.46 \end{bmatrix}$

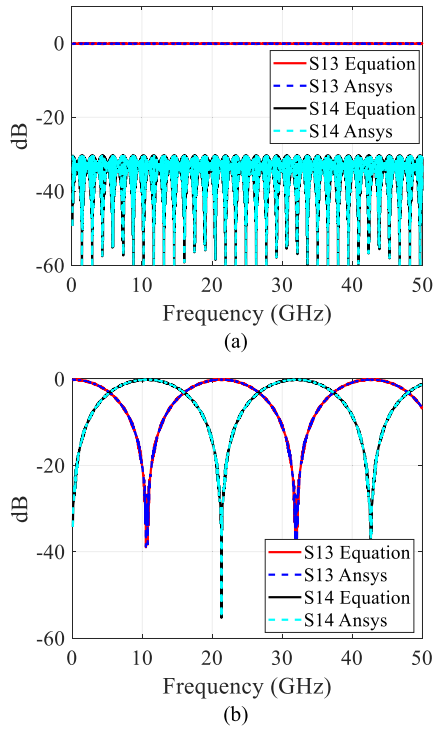

Fig. 4. Simulated and calculated *S*-parameters for the two test geometries in Fig. 3. (a) Without air pockets. (b) With air pockets.

The analysis presented in the previous section is supported by the simulation results. For the case with a homogeneous dielectric, the insertion loss is close to 0 dB, and the far-end crosstalk is below −30 dB. However, in the case with inhomogeneity, both the insertion loss and far-end crosstalk are periodic due to the modulation effect. Despite the small difference in the C matrix, a significant deviation is observed between the *S*-parameters of the two geometries, thus verifying the accuracy of the analysis. Notably, using (32), the frequency of the first zero in the insertion loss can be calculated, which is one-quarter of the modulation frequency, i.e., 10.67 GHz. The simulation result of 10.54 GHz shows only a 1% deviation from the calculated value, further validating the proposed analysis.

The insertion loss of the test geometry with air pockets for 0.1, 0.2, 0.5, and 1 m cables is compared in Fig. 5. Of note, the modulation frequency is inversely proportional to the length of the transmission line. As predicted by (32), the modulation frequency is lower for shorter cables.

In the case of cables with low-loss dielectric, the behavior of the *S*-parameters is similar to that in the lossless scenario,

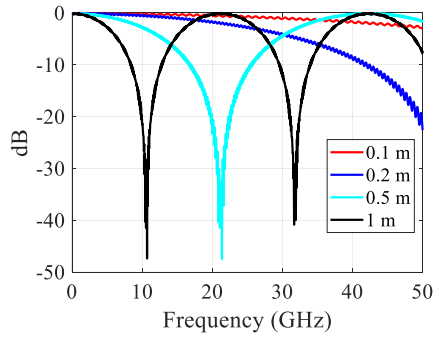

Fig. 5. Insertion loss for cables of various lengths with air pockets.

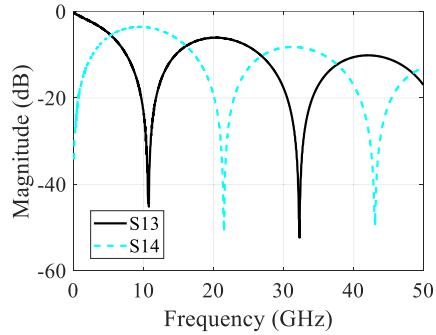

Fig. 6. S-parameter for a lossy cable with air pockets.

except for the presence of attenuation. To demonstrate this, the same geometry with air pockets using both copper and a lossy dielectric is simulated. The conductivity of copper is 5.8 e7S/m, and the lossy dielectric is defined by the Djordjevic-Sarkar model [20] with dk = 2.1 and df = 0.002 at 1 GHz. The simulated *S*-parameters are plotted in Fig. 6, which shows the same modulation pattern as that in the lossless case. The first zero in the insertion loss is 10.75 GHz, indicating a change of only 2% with respect to the lossless case.

Despite the difference in the single-ended *S*-parameters, the differential mode S-parameter for the two test geometries is the same. However, air pockets are beneficial if asymmetry-induced skew exists.

V. Analysis of Skew

A. Numerical Examples

The same test geometries in Fig. 3 are used as an example to illustrate the effect of inhomogeneity on skew. A cylinder with a dk value of 3.2 and 10 mil diameter is added 31 mil away, to the left of conductor 1, as shown in Fig. 7. The added cylinder makes the cross-section asymmetric and induces skew to the cables. The geometries are simulated in ANSYS 2D Extractor, and the simulated $\boldsymbol{L}$ and $\boldsymbol{C}$ matrices are listed in Table II. C_{11} increases slightly because the cylinder has a higher dk value than the dielectric. The *S*-parameters are calculated from the RLGC parameters with (20).

The frequency-domain intrapair skew is defined by the difference between the flight times of conductors 1 and 2, when a differential signal is fed into one end of the cable [4], [19].

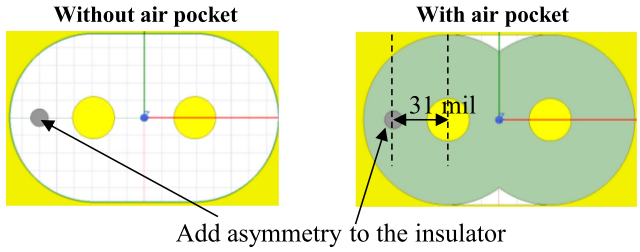

Fig. 7. Addition of skew to the test geometries for a twin-axial cable with and without air pockets.

TABLE II
Simulated **L** and **C** Matrix With Asymmetry

	$\boldsymbol{L}$ matrix (nH/m)	$\boldsymbol{C}$ matrix (pF/m)
Without air pockets	$\begin{bmatrix} 296.0 & 50.1 \\ 50.1 & 296.0 \end{bmatrix}$	$\begin{bmatrix} 81.59 & -13.75 \\ -13.75 & 81.26 \end{bmatrix}$
With air pockets	$\begin{bmatrix} 296.0 & 50.1 \\ 50.1 & 296.0 \end{bmatrix}$	$\begin{bmatrix} 80.80 & -14.38 \\ -14.38 & 80.46 \end{bmatrix}$

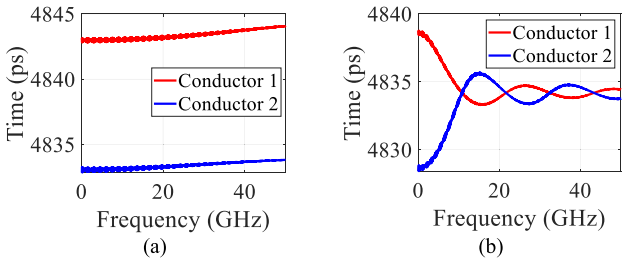

Fig. 8. Flight times of the two conductors. (a) Without air pockets. (b) With air pockets.

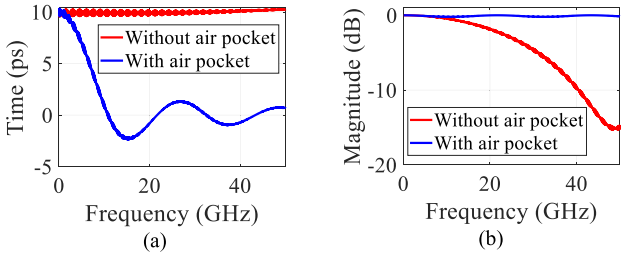

Fig. 9. Inhomogeneity decreases skew at high frequencies and removes the resonance on the differential insertion loss. (a) Intra-pair skew. (b) Differential insertion loss.

The flight time is defined as the time required by the signal to travel on the length of the conductor. The flight times of the two conductors t_1 and t_2 can be obtained from the *S*-parameters

$$t_1 = \text{unwrap}\left(\text{phase}\left(S_{31} - S_{32}\right)\right) \tag{39}$$

$$t_2 = \text{unwrap}\left(\text{phase}\left(S_{42} - S_{41}\right)\right). \tag{40}$$

The intrapair skew is the difference between t_1 and t_2

$$\text{skew} = |t_2 - t_1|. \tag{41}$$

Fig. 8 shows the calculated flight time, while Fig. 9(a) plots the skew and Fig. 9(b) plots the differential insertion loss. Additionally, Fig. 10 displays the time-domain transmission (TDT) waveform with a 25 ps rise time. For the co-extruded

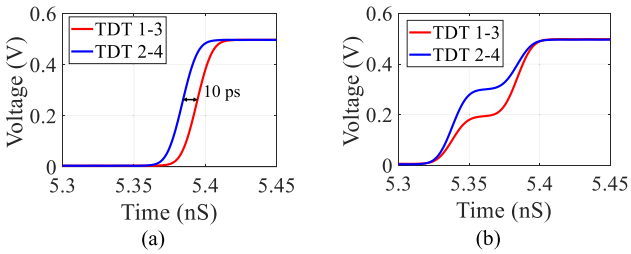

Fig. 10. TDT waveform with 25 ps rise time. (a) Without air pockets. (b) With air pockets.

cable without air pockets, the flight time varies little with frequency, and the skew remains at 10 ps across all frequencies. The skew leads to resonance on the differential insertion loss at $1/(2\text{skew}) = 50$ GHz. Notably, the TDT waveforms of the two conductors display a clear 10 ps difference.

For the case with air pockets, the flight time changes with the frequency. The skew starts with 10 ps at low frequency, then decreases to 0 ps at 10.7 GHz, which is one-quarter of the modulation period. Above 10.7 GHz, the skew oscillates around 0, and the sign changes with every half modulation period. The difference between the TDT waveforms is small around the corner where the high-frequency component is strong, and the difference is large at the middle of the rising edge where the low-frequency component is strong. The air pockets reduce the negative effect of skew on signal integrity.

B. Physical Explanation for Co-Extruded Cable With Skew

For a lossless co-extruded cable with an asymmetric dielectric, as shown in Fig. 7, the $\boldsymbol{C}$ matrix can be written as

$$\boldsymbol{C} = \begin{bmatrix} C_{11} + \delta C & C_{12} \\ C_{21} & C_{22} \end{bmatrix} \tag{42}$$

where $\delta C = 0.33\ \text{pF/m}$ is the perturbation due to the asymmetry calculated by the simulation result. The $\boldsymbol{P}$ matrix becomes

$$\begin{aligned} \boldsymbol{P} &= s^2 \boldsymbol{LC} = \\ & s^2 \begin{bmatrix} L_{11}C_{11} + L_{12}C_{21} + L_{11}\delta C & L_{12}C_{12} + L_{12}C_{22} \\ L_{21}C_{11} + L_{22}C_{21} + L_{21}\delta C & L_{21}C_{12} + L_{22}C_{22} \end{bmatrix} \\ &= s^2 \begin{bmatrix} L_{11}C_{11} + L_{12}C_{21} + L_{11}\delta C & 0 \\ L_{21}\delta C & L_{21}C_{12} + L_{22}C_{22} \end{bmatrix}. \end{aligned} \tag{43}$$

The new propagation constants are

$$\begin{aligned} \gamma_1 &= s\sqrt{L_{11}C_{11} + L_{12}C_{21} + L_{11}dC} \approx \gamma + \frac{s^2 L_{11}\delta C}{2\sqrt{\gamma}} \\ &= \gamma + \delta\gamma \end{aligned} \tag{44}$$

$$\gamma_2 = s\sqrt{L_{21}C_{12} + L_{22}C_{22}} = \gamma \tag{45}$$

where $\delta\gamma$ is the perturbation due to the asymmetry. The new $\boldsymbol{ABCD}$ matrix can be written as

$$\boldsymbol{A} = \begin{bmatrix} \cos h(\gamma_1 x) & 0 \\ 0 & \cos h(\gamma_2 x) \end{bmatrix} \tag{46}$$

$$\boldsymbol{B} = \begin{bmatrix} \frac{\sin h(\gamma_1 x)}{\gamma_1} & 0 \\ 0 & \frac{\sin h(\gamma_2 x)}{\gamma_2} \end{bmatrix} \begin{bmatrix} sL_{11} & sL_{12} \\ sL_{21} & sL_{22} \end{bmatrix} \tag{47}$$

$$\boldsymbol{C} = \begin{bmatrix} sL_{11} & sL_{12} \\ sL_{21} & sL_{22} \end{bmatrix}^{-1} \begin{bmatrix} \gamma_1 \sin h(\gamma_1 x) & 0 \\ 0 & \gamma_2 \sin h(\gamma_2 x) \end{bmatrix} \tag{48}$$

$$\begin{aligned} \boldsymbol{D} = & \begin{bmatrix} sL_{11} & sL_{12} \\ sL_{21} & sL_{22} \end{bmatrix}^{-1} \\ & \begin{bmatrix} \cos h(\gamma_1 x) & 0 \\ 0 & \cosh(\gamma_2 x) \end{bmatrix} \begin{bmatrix} sL_{11} & sL_{12} \\ sL_{21} & sL_{22} \end{bmatrix}. \end{aligned} \tag{49}$$

In contrast to the air pockets, the asymmetry does not lead to a modulation in $\boldsymbol{ABCD}$ parameters as in (33)–(35). Thus, no modulation behavior is seen in the single-ended S-parameters. For the same reason, the flight times of the two conductors are not significantly dependent on the frequency. The difference between propagation constants leads to resonances on the differential insertion loss. The resonant frequencies are inversely proportional to δC

$$f_{\text{resonance}} = \frac{(2n+1)\,\gamma}{\text{length} \times L_{11}\delta C}, n = 0, 1, 2 \ldots. \tag{50}$$

In this example, the first resonance calculated by (50) is 50 GHz, in agreement with the simulated results in Fig. 9, thus verifying the proposed explanations.

C. Explanation for Separately Extruded Cable With Skew

For a lossless separately extruded cable with an asymmetric dielectric and air pockets, as shown in Fig. 7, the $\boldsymbol{C}$ matrix can be written as

$$\boldsymbol{C} = \begin{bmatrix} C_{11} + \delta C & C_{12} \\ C_{21} & C_{22} \end{bmatrix} \tag{51}$$

where $\delta C = 0.33\ \text{pF/m}$ is the perturbation due to the asymmetry and is a small number. The $\boldsymbol{P}$ matrix becomes

$$\boldsymbol{P} = s^2 LC = \begin{bmatrix} p + s^2 L_{11}\delta C & e \\ e + s^2 L_{22}\delta C & p \end{bmatrix}. \tag{52}$$

Considering the perturbation due to the asymmetry is minor, on the basis of the assumption that $e >> s^2 L_{22}\delta C$, the new propagation constants γ_1'' and γ_2'' can be derived as

$$\begin{aligned} \gamma_1'' &\approx \sqrt{p - e - \frac{s^2 L_{22}\delta C}{2}} \approx \sqrt{p-e} - \frac{s^2 L_{22}\delta C}{4\sqrt{p-e}} \\ &\approx \gamma'_1 - \frac{s^2 L_{22}\delta C}{4\sqrt{p}} \end{aligned} \tag{53}$$

$$\begin{aligned} \gamma_2'' &\approx \sqrt{p + e + \frac{s^2 L_{22}\delta C}{2}} \approx \sqrt{p+e} + \frac{s^2 L_{22}\delta C}{4\sqrt{p+e}} \\ &\approx \gamma'_2 + \frac{s^2 L_{22}\delta C'}{4\sqrt{p}} \end{aligned} \tag{54}$$

where γ'_1 and γ'_2 are the same as those in (31) for a separately extruded cable without skew. Compared with the homogeneous and symmetrical geometry in Fig. 3, two factors affect the two propagation constants: air pockets and skew. The effect of the

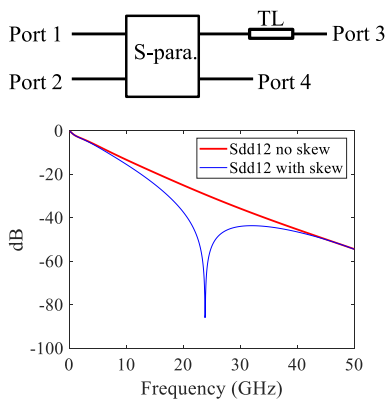

Fig. 11. Differential insertion loss Sdd_{12} with resonance for the symmetric separately extruded cable.

air pockets on the propagation constants is significantly greater than the effect of skew

$$|\gamma_1'' - \gamma'_1| \approx \left|\frac{s^2 L_{22}\delta C}{4\sqrt{p}}\right| << \left|\frac{e}{2\sqrt{p}}\right| \approx |\gamma'_1 - \gamma| \qquad (55)$$

$$|\gamma_2'' - \gamma'_2| \approx \left|\frac{s^2 L_{22}\delta C}{4\sqrt{p}}\right| << \left|\frac{e}{2\sqrt{p}}\right| \approx |\gamma'_2 - \gamma|\,. \qquad (56)$$

Consequently, adding skew does not change the modulation behavior caused by the air pockets. The magnitude of the single-end S-parameter remains unchanged after the addition of skew. The skew exists and causes a difference between the flight times at low frequencies. The sign of the difference changes with the frequency because of the modulation. Therefore, the skew calculated from the unwrapped phase is decreased at a high frequency after several modulation cycles.

D. Skew Due to Physical Length Difference

Of note, if the skew is caused by a difference in the physical lengths of the two conductors, the resonance will still be present at a frequency equal to 1/(2 skew) even with the air pockets as additional inhomogeneities. For verification, the S-parameter of the symmetric separately extruded cable in Fig. 4(b) is connected to an additional ideal delayed transmission line with a 21 ps delay at port 3, as shown in Fig. 11. Consequently, the differential insertion loss Sdd_{12} has a resonance at 23.8 GHz caused by the delay. Therefore, in the manufacturing copper twinax cables, the physical lengths of the two inner conductors must be precisely controlled.

VI. Conclusion

Separately extruded twinax cables often have lower manufacturing costs than co-extruded twinax cables. However, low cost does not always mean inferior performance. The skew-induced resonance in differential insertion loss is observable in the separately extruded twinax cables. Therefore, the higher skew does not undermine signal integrity if the skew is caused by inhomogeneity of the dielectric along the propagation direction. This inhomogeneity, which can arise from air pockets separately extruded cables within the cable, can cause modulation between propagation constants, reducing skew at high frequencies and eliminating the resonance in differential insertion loss.

The analysis presented in this article has implications beyond twinax cables and could be applied to other two-dimensional transmission lines. For example, intentional inhomogeneity in the dielectric material could be used to reduce crosstalk between two single-ended microstrips or striplines in printed circuit board design.

References

[1] *IEEE Standard for Ethernet Amendment 2: Physical Layer Specifications and Management Parameters for 100 Gb/s Operation Over Backplanes and Copper Cables*, IEEE Std 802.3bj-2014 (Amendment to IEEE Std 802.3-2012 as amended by IEEE Std 802.3bk-2013), pp. 1–368, Sep. 2014.

[2] T. Sugiyama, H. Nonen, I. Fukasaku, H. Ishikawa, and T. Kumakura, "High-speed transmission copper cable for 25Gbit/s/lane," in *Proc. 3rd IEEE CPMT Symp. Jpn.*, 2013, pp. 1–4.

[3] D. Nozadze, A. Koul, K. Nalla, M. Sapozhnikov, and V. Khilkevich, "Effective channel budget technique for high-speed channels due to differential P/N skew," in *Proc. IEEE Int. Symp. Electromagn. Compat. Signal/Power Integrity*, 2017, pp. 34–39.

[4] E. Mayevskiy and H. James, "Limitations of the intra-pair skew measurements in gigabit range interconnects," DesignCon, 2016.

[5] Z. Chen, M. Prasad, D. O'Connor, P. Bond, and A. Muszynski, "Differential twinax cable modeling by measured 4-port *S*-parameters," in *Proc. IEEE 14th Topical Meeting Elect. Perform. Electron. Packag.*, 2005, pp. 87–90.

[6] D. N. de Araujo, G. Pitner, M. Commens, B. Mutnury, and J. Diepenbrock, "Full-wave, twinax, differential cable modeling," in *Proc. 58th Electron. Compon. Technol. Conf.*, 2008, pp. 1684–689.

[7] Y. Shlepnev and C. Nwachukwu, "Modelling jitter induced by fibre weave effect in PCB dielectrics," in *Proc. IEEE Int. Symp. Electromagn. Compat.*, 2014, pp. 803–808.

[8] A. Talebzadeh et al., "SI and EMI performance comparison of standard QSFP and flyover QSFP connectors for 56+ Gbps applications," in *Proc. IEEE Int. Symp. Electromagn. Compat. Signal/Power Integrity*, 2017, pp. 776–781.

[9] Y. Liu et al., "Far-end crosstalk analysis for stripline with inhomogeneous dielectric layers (IDL)," in *Proc. IEEE Int. Joint EMC/SI/PI EMC Europe Symp.*, 2021, pp. 825–830.

[10] Y. Liu et al., "An empirical modeling of far-end crosstalk and insertion loss in microstrip lines," *IEEE Trans. Signal Power Integrity*, vol. 1, pp. 130–139, 2022.

[11] E. J. Denlinger, "Frequency dependence of a coupled pair of microstrip lines (correspondence)," *IEEE Trans. Microw. Theory Techn.*, vol. 18, no. 10, pp. 731–733, Oct. 1970.

[12] S. Yong, K. Cai, B. Sen, J. Fan, V. Khilkevich, and C. Sui, "A comprehensive and practical way to look at crosstalk for transmission lines with mismatched terminals," in *Proc. IEEE Symp. Electromagn. Compat., Signal Integrity Power Integrity*, 2018, pp. 538–543.

[13] S. Yong et al., "Dielectric loss tangent extraction using modal measurements and 2-D cross-sectional analysis for multilayer PCBs," *IEEE Trans. Electromagn. Compat.*, vol. 62, no. 4, pp. 1278–1292, Aug. 2020.

[14] N. Dikhaminjia, J. Rogava, M. Tsiklauri, M. Zvonkin, J. Fan, and J. L. Drewniak, "Fast approximation of sine and cosine hyperbolic functions for the calculation of the transmission matrix of a multiconductor transmission line," *IEEE Trans. Electromagn. Compat.*, vol. 57, no. 6, pp. 1698–1704, Dec. 2015.

[15] A. A. Bhatti, "A computer based method for computing the N-dimensional generalized ABCD parameter matrix of N-dimensional systems with distributed parameters," in *Proc. 22nd Southeastern Symp. Syst. Theory*, 1990, pp. 590–593.

[16] W. I. Bowman and J. M. McNamee, "Development of equivalent Pi and T matrix circuits for long untransposed transmission lines," *IEEE Trans. Power App. Syst.*, vol. 83, no. 6, pp. 625–632, Jun. 1964.

[17] D. M. Pozar, *Microwave Engineering*, 2nd ed. Hoboken, NJ, USA: Wiley, 1998.

[18] "Ansys electronics 2D extractor solver," 2023. [Online]. Available: https://www.ansys.com/products/electronics/option-2d-extractor-solver

[19] S. Baek, E. Lee, and B. Sung, "Computation of intra-pair skew for imbalance differential line using modified mixed-mode S-parameter," in *Proc. IEEE Elect. Perform. Electron. Packag.*, 2007, pp. 179–182.
[20] A. R. Djordjevic, R. M. Biljie, V. D. Likar-Smiljanic, and T. K. Sarkar, "Wideband frequency-domain characterization of FR-4 and time-domain causality," *IEEE Trans. Electromagn. Compat.*, vol. 43, no. 4, pp. 662–667, Nov. 2001.

Yuanzhuo Liu (Student Member, IEEE) received the B.E. degree in electrical and computer engineering from Huazhong University of Science and Technology, Wuhan, China, in 2017, and the M.S. degree in electrical engineering, in 2019, from Missouri University of Science and Technology (formerly University of Missouri−Rolla), Rolla, MO, USA, where she is currently working toward the Ph.D. degree in electrical engineering with EMC Laboratory.

Her research interests include signal integrity, electromagnetic interference, radio frequency defense, noise, and jitter analysis in high-speed digital systems.

Dr. Liu is the recipient of 2022 IEEE Electromagnetic Compatibility Society President's Memorial Award, DesignCon 2022 Early Career Best Paper Award, and Best SIPI Student Paper Award of 2021 IEEE International Joint EMC/SI/PI and EMC Europe Symposium.

Siqi Bai (Student Member, IEEE) received the B.S. degree in optoelectronic information engineering from Huazhong University of Science and Technology, Wuhan, China, in 2015, and the M.S. degree in electrical engineering in 2018 from Missouri University of Science and Technology (Missouri S&T), Rolla, MO, USA, where he is currently working toward the Ph.D. degree in electrical engineering with the Electromagnetic Compatibility Laboratory.

His research interests include PDN modeling and design, signal integrity, and automotive electromagnetic interference (EMI).

Dr. Bai was the recipient of the 2020 DesignCon best paper award and a recipient of the 2020 IEEE International Symposium on EMC best student paper award.

Chaofeng Li (Student Member, IEEE) received the B.S. degree in electronic science and technology from Guilin University of Electronic Technology, Guilin, China, in 2016, and the M.S. degree in electromagnetic field and microwave technology from the University of Electronic Science and Technology of China, Chengdu, China, in 2019. He is currently working toward the Ph.D. degree in electrical engineering from Missouri University of Science and Technology (formerly University of Missouri - Rolla), Rolla, MO, USA.

His current research interests include signal integrity, equivalent modeling for high-speed channel, material characterization method, and chip-PDN impedance modeling.

Vanine Sabino De Moura (Student Member, IEEE) received the B.Sc. and M.Sc. degrees in electrical engineering from the Universidade Federal de Pernambuco, Recife, Brazil, in 2014 and 2016, respectively. She is currently working toward the Ph.D. degree in electrical engineering with the EMC Laboratory, Missouri University of Science and Technology, Rolla, MO, USA.

Her research interests include antenna design and analysis, signal integrity, and numerical methods in electromagnetics.

Bichen Chen (Member, IEEE) received the M.S. degree in electrical and computer engineering from Tandon School of Engineering, New York University, Brooklyn, NY, USA, in 2012, and the Ph.D. degree in electrical engineering from Missouri University of Science and Technology (formerly University of Missouri-Rolla), Rolla, MO, USA, in 2019.

He is currently a Network Hardware Engineer with Facebook, Inc., Menlo Park, CA, USA, where he works on SI/PI of networking hardware for Facebook's megascale data centers.

Srinivas Venkataraman received the M.S. degree in electrical engineering from the University of Arizona, Tucson, AZ, USA, in 1994.

He is currently a Signal Integrity Engineer with Facebook, Menlo Park, CA, USA, working on next-generation switches for Facebook's hyperscale data centers. Prior to his position at Facebook, he was the Director of hardware engineering with Juniper Networks, Sunnyvale, CA, USA, leading a team of engineers in designing systems with high-speed interconnects for multiple generations of core and edge-routing products. Previously, he was with Hewlett Packard, Palo Alto, CA, USA, on fault-tolerant systems and with Intel on IA64 processors for package and system signal integrity solutions.

Xu Wang received the B.S. and M.S. degrees in electrical engineering from Tsinghua University, Beijing, China, in 1994 and 1996.

He is currently a Hardware Engineer with Facebook, Inc., Menlo Park, CA, USA, where he works on system-level design and validation of networking hardware for Facebook's megascale data centers. Prior to joining Facebook, he designed enterprise firewall products with Fortinet, Sunnyvale, CA, USA, for system-level and board-level hardware. Previously, he was a Hardware Manager and a Hardware Engineer with Ribbon Communications, Plano, TX, USA, for more than 10 years on VoIP media gateways.

DongHyun Kim (Member, IEEE) received the B.S., M.S., and Ph.D. degrees in electrical engineering from the KAIST, Daejeon, Republic of Korea, in 2012, 2014, and 2018, respectively.

In 2018, he joined Missouri S&T (formerly University of Missouri-Rolla), Rolla, MO, USA, and he is currently an Assistant Professor with the EMC Laboratory, Missouri S&T, Rolla, MO, USA. His current research interests include nanometer-scale devices, through-silicon via technology and signal integrity, power integrity, temperature integrity, electromagnetic compatibility, and electrostatic discharge in 2.5D/3D IC systems.